Compact spherical neutron polarimeter using high-T_c YBCO films

T. Wang, S. R. Parnell, W. A. Hamilton, F. Li, A. L. Washington, D. V. Baxter, and R. Pynn

Citation: Review of Scientific Instruments **87**, 033901 (2016); doi: 10.1063/1.4943254
View online: http://dx.doi.org/10.1063/1.4943254
View Table of Contents: http://aip.scitation.org/toc/rsi/87/3
Published by the American Institute of Physics

Compact spherical neutron polarimeter using high-T_c YBCO films

T. Wang,[1] S. R. Parnell,[1,2] W. A. Hamilton,[3] F. Li,[1] A. L. Washington,[4] D. V. Baxter,[1] and R. Pynn[1,3]

[1]*Center for Exploration of Energy and Matter, Indiana University Bloomington, Bloomington, Indiana 47408, USA*
[2]*Faculty of Applied Sciences, Delft University of Technology, Mekelweg 15, 2629 JB Delft, The Netherlands*
[3]*Neutron Science Directorate, Oak Ridge National Laboratory, Oak Ridge, Tennessee 37381, USA*
[4]*Department of Physics and Astronomy, The University of Sheffield, Sheffield S10 2TN, United Kingdom*

(Received 12 November 2015; accepted 20 February 2016; published online 14 March 2016)

We describe a simple, compact device for spherical neutron polarimetry measurements at small neutron scattering angles. The device consists of a sample chamber with very low (<0.01 G) magnetic field flanked by regions within which the neutron polarization can be manipulated in a controlled manner. This allows any selected initial and final polarization direction of the neutrons to be obtained. We have constructed a prototype device using high-T_c superconducting films and mu-metal to isolate regions with different magnetic fields and tested device performance in transmission geometry. Finite-element methods were used to simulate the device's field profile and these have been verified by experiment using a small solenoid as a test sample. Measurements are reported using both monochromatic and polychromatic neutron sources. The results show that the device is capable of extracting sample information and distinguishing small angular variations of the sample magnetic field. As a more realistic test, we present results on the characterization of a 10 μm thick Permalloy film in zero magnetic field, as well as its response to an external magnetic field. [http://dx.doi.org/10.1063/1.4943254]

I. INTRODUCTION

Neutrons can be used to study both magnetic[1] and atomic[2] structures in materials. The sensitivity to magnetic structure arises from the interaction of the magnetic moment of the neutron with magnetic fields within a sample that result from the presence of unpaired electrons. This dipolar interaction results in scattering that is sensitive only to the component of the microscopic sample magnetisation perpendicular to the neutron scattering vector **Q**. The magnetic scattering cross section depends in a complicated way on the direction of the neutron polarization before and after scattering. The behaviour of the polarization dependence of the scattering can be expressed as a tensor described by Brown,[3] which is based on the initial derivations by Maleyev[4] and Blume[5] and draws on the earlier paper of Halpern and Johnson.[6] Measurements of this polarization dependence in diffraction experiments have yielded important information about the coupling of lattice distortion and magnetism and about chiral magnetic structure, which are not accessible through other techniques.[7]

Polarization analysis in its simplest form is commonly referred either as 1-D polarization analysis or longitudinal polarization analysis, because the initial and final neutron polarizations are analyzed with respect only to the direction of the magnetic field applied to the sample. With the polarization **P** aligned along the neutron scattering vector, this method can be used to separate the magnetic and nuclear contributions to the scattering.[2,8,9] The polarization analysis technique can be further developed by changing the relative orientation of **Q** and **P** by rotating the magnetic guide field that controls the direction of **P**. In this way, polarization analysis can be used to determine the orientation of magnetic moments,[10] or to study paramagnetic scattering as shown by Moon *et al.*[2,11] It was not until the advent of large-area supermirror analyzers[12] that dedicated instruments were built[13] where three mutually perpendicular Helmholtz coils at the sample position allowed the neutron polarization to be measured simultaneously over a wide range of **Q**. Such measurements, commonly known as xyz polarization analysis, allow the separation of the nuclear coherent, nuclear spin incoherent and magnetic scattering[14] terms both for wide angle diffraction and Small Angle Neutron Scattering (SANS).[15] However, none of the techniques above can be used to determine the off-axis components of the polarization tensor as both the initial and final polarization directions are parallel to one another and to the magnetic guide field applied to the scattering sample. The off-axis components can be determined by the use of the Spherical Neutron Polarimetry (SNP) technique that decouples the incident and scattered beam polarization directions with the use of a zero-field chamber at the sample position. Currently available SNP devices include CryoPAD[16] which operates at ILL (France), FRM II (Germany), and JAERI (Japan) and MuPAD[17] which operates at FRM II and SINQ (Switzerland). There is also a newly developed miniaturized version of MuPAD (the so-called "MiniMuPAD") at Technische Universität München[18] that is suitable for polarization analysis in transmission or SANS geometry. Examples of SNP measurements include measuring the form factor of an antiferromagnet in zero field[19] and extracting the structure of multi-domain systems. More recently a SNP device has also been used to study chiral systems in both elastic[7] and inelastic scattering.[20] The application extends to broad fields including multiferroics,[21,22] heavy fermions,[23] and superconductors.[24] Currently most SNP

measurements have focused on diffraction; however, the technique can also be used for 3D neutron depolarization[25] and inelastic scattering.

In CryoPAD, superconducting niobium screens are used either for non-adiabatic neutron spin manipulation or to enclose a region of zero magnetic field. When used for spin manipulation, a Meissner sheet cleanly separates two regions with differently directed magnetic fields, both of which are parallel to the sheet, allowing neutron spin precession to be started abruptly and in a controlled manner as the neutron passes through the sheet. With a combination of adiabatic rotation and precession, the neutron polarization vector can be placed into any desired direction when preparing the incident beam and analyzing the scattered beam. In MuPAD, a set of two orthogonal solenoids is used to manipulate the spin through a combination of two precessions about two orthogonal axes. Both CryoPAD and MuPAD are relatively straightforward to use with monochromatic neutrons since the currents in the various precession devices need only be set once. The situation becomes more complex when time-of-flight methods are used to determine the wavelength of polychromatic neutron beams and, to our knowledge, there has been no successful use of either of these devices at a time-of-flight beamline. In principle, since the arrival time of neutrons of a given wavelength is known, it may be possible to use ramped magnetic fields[26] to manipulate the neutron polarization, but this has not been done.

Many time-of-flight neutron scattering instruments use detectors that cover a wide range of scattering angles, which complicates SNP. While polarization analyzers suitable for the broad angular coverage typical of time-of-flight measurements have recently become more widely available,[27] SNP measurements at pulsed neutron sources would still be more complex than they are at constant wavelength sources. The Blume-Maleyev polarization tensor[4,5] is defined relative to the scattering vector **Q**. This vector varies across a neutron detector with large angular coverage so the initial and final polarizations of the neutron cannot have simple orientation relationships with **Q** in all detector channels. A practical approach to a physical device that could be used to implement a wide angle CryoPAD suitable for TOF source has been presented by Lelièvre-Berna.[28] However the accuracy, effectiveness, and type of problem that could be addressed have not yet been fully explored to our knowledge.

Our goal in this paper is to present a device for SNP that is simpler and less expensive than its predecessors and can be used on a time-of-flight instrument with narrow angular coverage. In essence the device is a more compact and simplified version of the ILL CryoPAD. It uses high-T_c superconducting films of YBCO deposited on single-crystal sapphire substrates that we have already shown to provide a high flipping efficiency[29] and low SANS background when used to make a Cryoflipper.[30] We also use coils wound with high-T_c YBCO tape to reduce heating in the precession regions and cool the whole device using a closed cycle refrigerator (CCR), dispensing with the need for liquid cryogens.

II. DEVICE DESIGN AND CONSTRUCTION

This compact SNP device is designed to control the incoming and outgoing neutron polarization separately, while keeping the sample in zero magnetic field. The layout of the device is shown in Figure 1(a). It consists of a zero field sample chamber with a precession region on each side mounted inside a vacuum chamber. Four thin plates of single-crystal sapphire coated with YBCO are used as Meissner screens to create sharp non-adiabatic transitions for the neutron polarization as the neutron moves between the sample chamber and precession regions. All of the components are mounted to an oxygen-free copper frame cooled with a CCR to a temperature below the superconducting transition of YBCO (~90 K). Two rotatable guide fields, with magnetic fields perpendicular to the neutron beam, are mounted outside the vacuum chamber on each side. A schematic of a rotatable guide field is shown in Figure 1(b). These guide fields interface with two solenoid guide fields whose fields are along the neutron beam, allowing an adiabatic rotation of the neutron polarization. The vacuum chamber has a rectangular cross section to minimize the distance between each external rotatable guide field and the YBCO film closest to it.

The two precession regions contain vertical magnetic fields (parallel to the YBCO film plane of Figure 1(a)), which cause the component of the neutron polarization in the horizontal plane to precess. The precession fields are designed to align with each other, although their magnitudes are controlled separately. The lab coordinate system is defined by choosing the beam direction as the $\hat{y}$ axis and the precession field direction as the $\hat{z}$ axis so that the YBCO films are in the x-

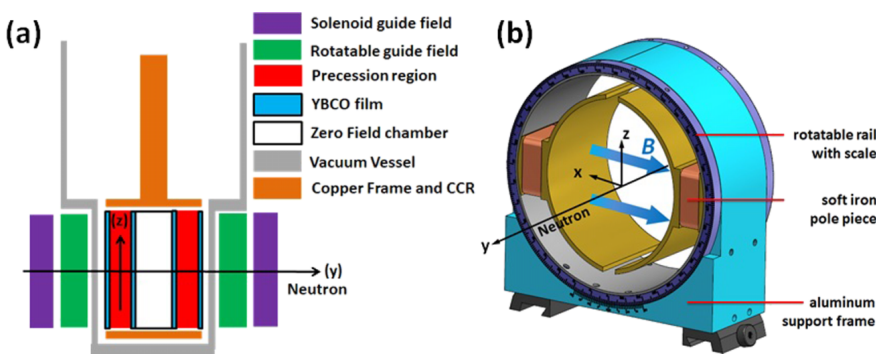

FIG. 1. (a) Layout of the device components. (b) Schematic of the rotatable guide field with the laboratory coordinates used throughout this paper.

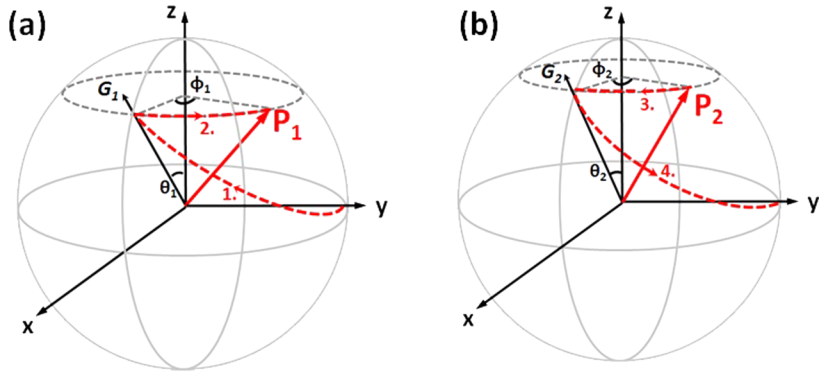

FIG. 2. Spin manipulation procedure for (a) incoming neutrons and (b) outgoing neutrons. On the incoming side, neutrons are initially polarized along the y direction, parallel to the direction of travel of the neutron beam. The polarization then changes adiabatically to a direction in the x-z plane as the neutron moves from the solenoid into a rotatable guide field. Finally, following a non-adiabatic transition through a high-T_c Meissner sheet, the neutron spin polarization vector undergoes Larmor precession to reach the desired orientation, labelled P_1 in (a). Control of the outgoing polarization follows a similar procedure, as shown in (b). The numbers 1–4 next to the dashed-line polarization trajectories in parts (a) and (b) refer to polarization changes described in the text.

z plane, orthogonal to the neutron propagation direction ($\hat{y}$). The two rotatable guide fields generate magnetic fields that are parallel to the adjacent YBCO film.

The change of neutron polarization during manipulation is shown in Figure 2. Preparation of the incoming polarization $\boldsymbol{P_1} = (\sin(\theta_1)\cos(\phi_1), \sin(\theta_1)\sin(\phi_1), \cos(\theta_1))$ can be described as follows:

1. The incoming neutron beam is polarized along $\hat{y}$ defined by the solenoid guide field. The polarization is adiabatically rotated to the field direction of the incident-beam rotatable guide field direction $\boldsymbol{G_1} = (\sin(\theta_1), 0, \cos(\theta_1))$.
2. The incoming precession device rotates the neutron polarization around $\hat{z}$ by an angle ϕ_1 so that the desired incoming polarization $\boldsymbol{P_1}$ is achieved. This rotation is expressed as rotation matrix $\boldsymbol{R_1}(\phi_1)$.

   The selection of outgoing neutron's polarization is essentially a reversed version of the procedure used for the incident beam, where the selected outgoing polarization along $\boldsymbol{P_2} = (\sin(\theta_2)\cos(\phi_2), \sin(\theta_2)\sin(\phi_2), \cos(\theta_2))$ is preserved.
3. The selected polarization direction $\boldsymbol{P_2}$ of the outgoing neutron is rotated inside the outgoing precession region by an angle of ϕ_2, so that it is set into the x-z plane. This rotation is expressed as rotation matrix $\boldsymbol{R_2}(\phi_2)$. The outgoing guide field is set along direction $\boldsymbol{G_2} = (\sin(\theta_2), 0, \cos(\theta_2))$, so that the selected polarization is completely projected onto the guide field when neutron passes through the Meissner shield.
4. After passing through the Meissner shield, the selected final polarization is preserved and then adiabatically rotated to the $\hat{y}$ direction.

From the Blume equation,[31] the change of the neutron spin polarization caused by the sample can be generalized as $\boldsymbol{P_2} = \boldsymbol{T_s}\cdot\boldsymbol{P_1} + \boldsymbol{P'}$, where $\boldsymbol{T_s}$ is the 3×3 Blume and Maleyev[4,5] tensor that describes the rotation of neutron polarization and $\boldsymbol{P'}$ is the polarization generated by the sample. Through manipulating $\boldsymbol{P_1}$ and $\boldsymbol{P_2}$, our design can be used to extract each component of $\boldsymbol{T_s}$ and $\boldsymbol{P'}$ through a combination of measurements. Through steps 1 and 2, the incoming polarization $\boldsymbol{P_1}$ can be expressed as $\boldsymbol{P_1} = \boldsymbol{R_1}(\phi_1)\cdot\boldsymbol{G_1}\cdot P_{pol}$, where P_{pol} is the magnitude of polarization determined by the beamline polarizer. Through steps 3 and 4, the outgoing polarization is manipulated by $\boldsymbol{R_2}$ and $\boldsymbol{G_2}$ into the analyzing direction, so that the measured polarization magnitude becomes $P_{measured} = P_a\cdot\boldsymbol{G_2}\cdot\boldsymbol{R_2}(\phi_2)\cdot\boldsymbol{P_2}$, where P_a is the analyzing power of the analyzer. Substituting the expressions for P_1 and P_2 into $P_{measured}$, the measured polarization magnitude can be expressed as

$$P_{measured} = P_a\cdot\boldsymbol{G_2}\cdot\boldsymbol{R_2}(\phi_2)\cdot[\boldsymbol{T_s}\cdot\boldsymbol{R_1}(\phi_1)\cdot\boldsymbol{G_1}\cdot P_{pol} + \boldsymbol{P'}]. \quad (1a)$$

For the measurements in this paper, to simplify the calculation, we only considered purely magnetic interaction between neutrons and the sample so $\boldsymbol{P'} = \boldsymbol{0}$. In this case, we rewrite Eq. (1a) as

$$P_n = \boldsymbol{G_2}\cdot\boldsymbol{R_2}(\phi_2)\cdot\boldsymbol{T_s}\cdot\boldsymbol{R_1}(\phi_1)\cdot\boldsymbol{G_1}, \quad (1b)$$

where $P_n = P_{measured}/(P_a\cdot P_{pol})$ is defined as the normalized polarization. The normalized polarization is independent of the influence of polarizer and analyzer and changes solely due to the interaction with sample. The normalized polarization is calculated by dividing the measured polarization by the polarization of the empty beamline, which is determined by the polarizer and analyser efficiencies.

The zero-field sample chamber and two precession regions are magnetically isolated to exclude any external magnetic field. This is achieved through a combination of YBCO films and a mu-metal shield, as shown in Figure 3(a). Each region is enclosed between two pieces of YBCO film and a closed mu-metal yoke. The controlled vertical fields required inside the precession regions are generated by pairs of coils wound with superconducting YBCO tape to reduce Ohmic heating. In order to manipulate neutrons of wavelength 2 Å, the precession coils require up to 8 A of current. This much current would generate around 6 W using normal resistive wire, which is close to the CCR cooling power (6.7 W), and would cause the temperature to rise above the YBCO film transition temperature. This problem is completely avoided by using YBCO current-carrying tape. An exploded view of a precession region is shown in Figure 3(b). During the cooling of the device, we also place a mu-metal shielding around the vacuum chamber to greatly reduce any magnetic field trapped

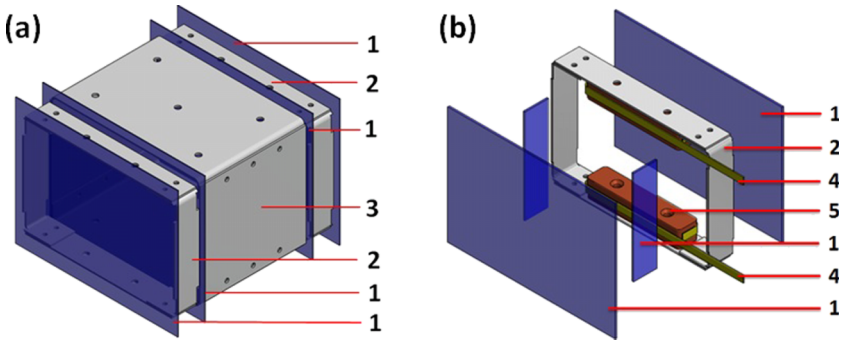

FIG. 3. (a) Schematic of precession region and sample chamber with only YBCO films and mu-metal visible. (b) Exploded view of a single precession region. The parts are numbered as 1—YBCO film; 2—precession region mu-metal; 3—zero-field chamber mu-metal; 4—superconducting coil; 5—copper coil core.

in the YBCO films when they are cooled through their superconducting transition.

III. DEVICE CALIBRATION

The prototype device was tested at the SESAME beamline on the Low Energy Neutron Source (LENS)[32,23] at Indiana University, and at the HB-2D beamline on the High Flux Isotope Reactor (HFIR), Oak Ridge National Laboratory. The SESAME beamline[33] provides a pulsed, polarized neutron beam with wavelengths in the range from 2 to 10 Å and polarization up to 92%. The neutrons are polarized using a supermirror bender[32] and the polarization is analysed using a continuously pumped ^{3}He filter.[34] The HB-2D beamline at HFIR uses supermirror benders as both polarizer and analyser, giving an instrument polarization of 79.3% at a neutron wavelength of 2.67 Å. For the calibration we performed the measurement without a sample and therefore Eq. (1b) becomes $P_n = \boldsymbol{G_2}\cdot\boldsymbol{R_2}(\phi_2)\cdot\boldsymbol{R_1}(\phi_1)\cdot\boldsymbol{G_1}$. By measuring the normalized neutron polarization, we study the depolarization due only to our device.

A. Magnetic field orientation calibration

The two vectors $\boldsymbol{G_1}$ and $\boldsymbol{G_2}$ are defined by θ_1 and θ_2, which are the relative angles between the magnetic fields from each rotatable guide field and the $\hat{z}$ axis (as defined in Fig. 2). These angles are controlled by adjusting the direction of the rotatable guide fields. The calibration measurements are performed with one precession field turned on while the other precession field is turned off. In these configurations, one of the matrices $\boldsymbol{R_1}(\phi_1)$ or $\boldsymbol{R_2}(\phi_2)$ is a unit matrix while the other is a rotation matrix around $\hat{z}$. Eq. (1b) is therefore written as

$$P_n = \cos(\theta_1)\cos(\theta_2) + \sin(\theta_1)\cos(\phi_i)\sin(\theta_2), \qquad (2)$$

where $\phi_i = \phi_1$ or ϕ_2, depending on which precession field is turned on.

To determine θ_1 and θ_2, the precession angle ϕ_i is first calibrated as a function of applied current, and then the 90° and 0° positions for θ_1 and θ_2 are determined, allowing any other angles to be set accurately. Shown in Figure 4(a) is the measured polarization at LENS after the two rotatable guide fields are adjusted so that $\theta_1 = 90°$ and $\theta_2 = 0°$ with respect to the incoming precession field. Within the range of usable neutron wavelengths (2 Å–6 Å), the measured polarizations have an average polarization of 0.6%, while varying between −7.5% and 4%. The useable neutron band is determined by the intensity distribution of the SESAME beamline (as shown in the histogram in Figure 4(a)) and by the polarization performance of the supermirror bender and ^{3}He filter used as polarizer and analyser, respectively. Within the usable wavelength range, the Larmor precession rate varies between 2 rad/cm and 6 rad/cm

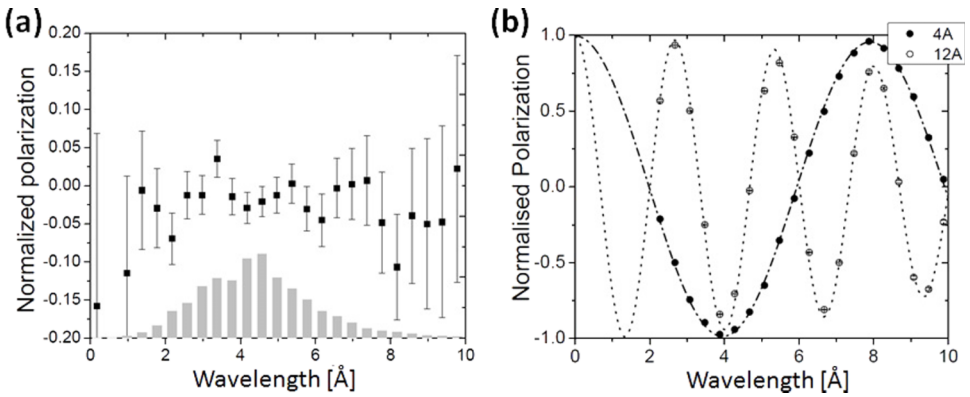

FIG. 4. (a) Normalized polarization (solid dots) as a function of wavelength after the two rotatable guide fields are adjusted so that $\theta_1 = 0°$ and $\theta_2 = 90°$. The intensity spectrum of the neutron beam is shown as the histogram, indicating that neutrons with wavelengths between 2 Å and 6 Å provide acceptable statistical errors at LENS for reasonable measurement times. (b) Normalized polarization as a function of wavelength for the incoming precession device with 4 A and 12 A current applied (points), using a 20×20 mm^2 beam, with fits to Eq. (4) (dashed lines).

in the guide fields, which is much larger than the rate of change of the guide field orientation of ~0.3 rad/cm. Therefore the transitions between the solenoid guide fields and the rotatable guide fields are adiabatic. During the calibration, we adjust the rotatable guide fields until the measured polarization is within 1% of the desired value, which corresponds to a maximum uncertainty of 0.8° for θ_1 and θ_2. Since our rotatable guide fields are relatively crude, they can only be set with accuracy around 1°, so the potential maximum errors in setting θ_1 and θ_2 are ~1.5°. However it should be noticed that for the measured data shown in Figure 4(a), the errors are dominated by the statistical errors rather than the accuracy of controlling θ_1 and θ_2. This is due to the fact that the low intensity of the SESAME beamline limits the number of counts that can be acquired within a reasonable time.

B. Precession calibration

The calibration in Section III A determines the value of θ_1 and θ_2. It also confirms that $\boldsymbol{R_1}(\phi_1)$ and $\boldsymbol{R_2}(\phi_2)$ are rotation matrices around the $\hat{z}$ axis. In the ideal case, the precession angles ϕ_1 and ϕ_2 are equal to the Larmor precession angle $\phi_L = \gamma_L Blm\lambda/h$, where B is the precession field strength and l is the length of the precession region. Since the field strength B is proportional to the current in the precession coil, the precession angle can be expressed as $\phi_L = \alpha I\lambda$ with $\alpha = \gamma_L Blm/Ih$, describing the precession angle generated per unit current per angstrom. Note that the YBCO films are parallel to one another by construction, so the path length through each precession region is constant across the neutron beam to a high degree of precision.

In reality, two potential imperfections need to be taken into consideration: the non-uniformity of the precession field and the coupling between the precession field and the neighbouring rotatable guide field. A slight spatial non-uniformity of the precession field will cause the precession coefficient α to depend on position within the neutron beam. Defining $\alpha(\vec{r}) = \bar{\alpha} + \Delta\alpha(\vec{r})$, where $\bar{\alpha}$ is the average value across the beam and $\Delta\alpha(\vec{r})$ is the deviation, the latter has been estimated using a finite-element method implemented in the commercially available code Magnet©, as shown in Figure 5(b). Since the simulation indicates that $\Delta\alpha(\vec{r})$ is small over the neutron beam, the matrix elements in the rotation matrix can be expanded and written as:

$$\boldsymbol{R} = \begin{bmatrix} (1-\beta\cdot I^2\lambda^2)\cos(\bar{\alpha}I\lambda) & (1-\beta\cdot I^2\lambda^2)\sin(\bar{\alpha}I\lambda) & 0 \\ -(1-\beta\cdot I^2\lambda^2)\sin(\bar{\alpha}I\lambda) & (1-\beta\cdot I^2\lambda^2)\cos(\bar{\alpha}I\lambda) & 0 \\ 0 & 0 & 1 \end{bmatrix}, \tag{3a}$$

where $\beta = \frac{1}{2}\int_{Beam}\Delta\alpha(\vec{r})^2 dS/\int_{Beam} dS$ is the dephasing coefficient, which expresses the decrease in neutron polarization caused by imperfections in the precession field regions.

Once again in the ideal case, the two vectors $\boldsymbol{G_1}$ and $\boldsymbol{G_2}$ can be written in the general form $\boldsymbol{G} = (\sin(\theta), 0, \cos(\theta))$. But in reality θ may vary across the neutron beam. The same finite element method described above was used to simulate the distribution of angles, shown in Figure 5(a). Treating the variation of theta as a small quantity and expanding the trigonometric functions yield

$$\boldsymbol{G} = \gamma\cdot(\sin(\theta), 0, \cos(\bar{\theta})), \tag{3b}$$

where $\theta(\vec{r}) = \bar{\theta} + \Delta\theta(\vec{r})$ and we define $\gamma = 1 - \frac{1}{2}\int_{Beam}\Delta\theta(\vec{r})^2 dS/\int_{Beam} dS$ as the field coupling coefficient. Notice that the field coupling coefficient $\gamma \leq 1$ and equals one when the precession device is turned off. Moreover, since γ depends on the variation of the angle distribution, it is independent of the average angle and neutron wavelength.

With Eqs. (3a) and (3b), the explicit form of $\boldsymbol{G}$ and $\boldsymbol{R}$ is established. However the three parameters α, β, and γ must be determined through calibration measurements. These were performed at the SESAME beamline at LENS, where the polychromatic neutrons can distinguish β and γ, because both factors cause depolarization but only β is wavelength dependent. To make the measurements, each of the two precession devices is calibrated individually and the two rotatable guide fields are both set to the $\hat{x}$ direction so that $\bar{\theta}_1 = \bar{\theta}_2 = 90°$. Substituting Eqs. (3a) and (3b) into Eq. (1b), the normalized polarization can therefore be expressed as

$$P_n = \gamma^2\cdot(1-\beta I^2\lambda^2)\cdot\cos(\bar{\alpha}I\lambda). \tag{4}$$

Experimental results for the incoming precession device with currents of 4 A and 12 A are shown as points in Figure 4(b). These results are fitted to Eq. (4), as shown by the dashed lines. The result for the outgoing precession device overlaps with the incoming precession device and therefore is

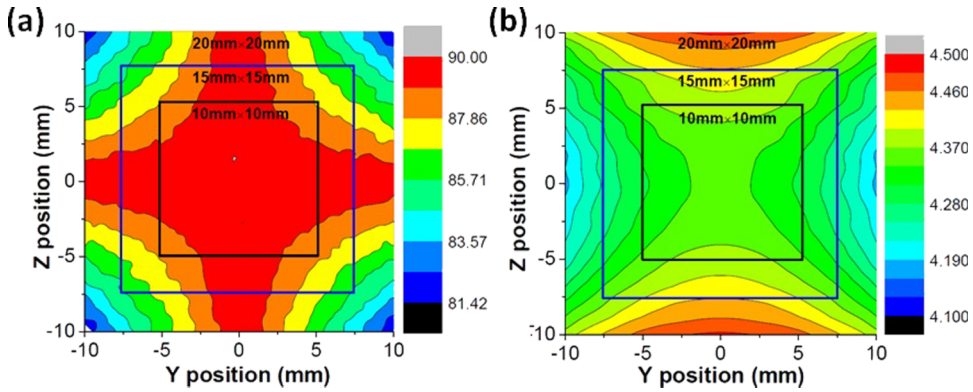

FIG. 5. Simulation result using a finite element method. (a) Mapping of the relative angle between the external guide field vectors and internal precession field vectors on each side of the YBCO films. (b) Mapping of the magnetic field integral in a precession region with 1 A current through the coils.

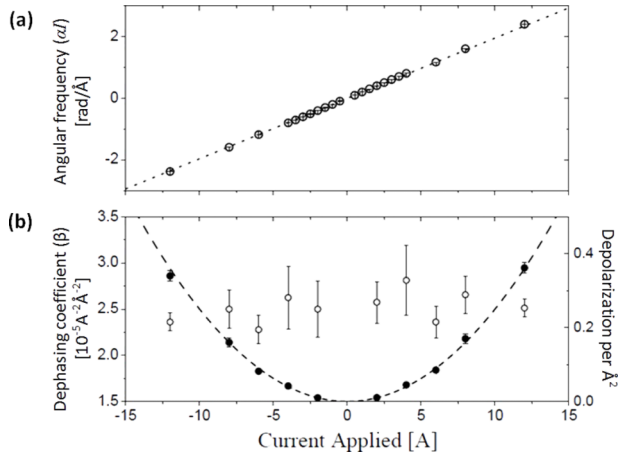

FIG. 6. (a) Precession angular frequency as a function of applied current through the incoming precession device (open circles) and a linear fit (dashed line), where the slope of the linear fit is the precession coefficient α. (b) The depolarization per neutron wavelength squared βI^2 (solid circles) and the extracted dephasing coefficient β (open circles) with 20×20 mm^2 beam size. The dashed line is a fit of βI^2 to a quadratic function.

omitted for clarity. The consistency of the fitting ensures that the three parameters α, β, and γ can be determined accurately.

From Eq. (4), the angular frequency of the fitted oscillation function is $\bar{\alpha} I$. Plotting the angular frequency as function of applied current, as shown in Figure 6(a), yields the precession coefficient α. The fitted line goes through zero and all data points fall on the line within their error bars, confirming that the precession is well controlled and stable across a wide range of applied current. The precession coefficients are almost identical for both incoming and outgoing precession devices and have values of $0.196 \pm 2 \times 10^{-4}$ (AÅ)$^{-1}$ and $0.193 \pm 2 \times 10^{-4}$ (AÅ)$^{-1}$, respectively. The finite element simulation predicts a precession coefficient $\alpha = 0.198 \pm 0.005$ (AÅ)$^{-1}$, consistent with the experimental results. Extrapolating the fitting of Eq. (4) to 0 Å, the zero point intercept value is 99.64% for a 20×20 mm^2 beam, which suggests that $\gamma^2 = 0.9964$ and the field coupling coefficient $\gamma = 0.9982$. This result is also consistent with the simulation result of 99.8% polarization transfer rate for the same beam size. Finally, the wavelength dependent depolarization $\beta I^2 \lambda^2$ divided by λ^2 is plotted as a function of applied current and shown as the solid points in Figure 6(b) together with a fit to a quadratic function. The extracted values of β are shown in Figure 6(b) at various currents applied through precession device. The fitted values are constant with small variations around 2.52×10^{-5} (AÅ)$^{-2}$, which is slightly better than the $\beta = 3.1 \times 10^{-5}$ (AÅ)$^{-2}$ result predicted by the finite element simulation. All parameters discussed above are the same for both incoming and outgoing precession devices within 2%, which is expected since the designs are identical.

IV. MEASURING THE MAGNETIC FIELD INSIDE A SOLENOID

After calibration, we used the device to measure the magnetic field inside a small solenoid that is 46.5 mm tall with a 27.4×28.4 mm^2 cross section. It is wound with aluminium wire and enclosed by a rectangular shaped mu-metal loop for magnetic flux return. Therefore, the solenoid can be treated as an infinitely long solenoid with a field of 12.5 G/A. The solenoid is mounted at the centre of the sample chamber with its internal field approximately parallel to the precession field direction ($\hat{z}$). The neutron beam passes through the centre of the solenoid perpendicular to its largest surface. Since the solenoid is purely magnetic and generates no additional polarization, we can once again use Eq. (1b) to describe the measured results. The Blume tensor for the sample solenoid is a 3×3 matrix with each matrix component labelled as T_{ij}, where "i" stands for the outgoing polarization and "j" stands for the incoming polarization. For measurements of the solenoid, it is convenient to set i, j = x, y, or z defined by the lab coordinate. Since the sample is a simple solenoid installed vertically, we expect T_{ij} to take the form of a rotation matrix around the $\hat{z}$ axis.

A. Monochromatic measurement

For a single neutron wavelength, the measurements are similar to the existing devices such as CryoPAD. The incoming and outgoing neutron polarizations are each set to one of the Cartesian (x, y, z) directions and the measured polarization is a direct measurement of one of the Blume tensor components of the sample. Substituting Eqs. (3a), (3b), and (4) into Eq. (1b), we obtain the relationship between the normalized polarization P_n and the Blume tensor components,

$$P_n = T_{ij} \quad \text{for } (i,j) = (x,x),(x,z),(z,x), \text{ and } (z,z), \tag{5a}$$

$$P_n = \gamma^2(1 - \beta \cdot I^2 \cdot \lambda^2)\, T_{ij} \quad \text{for } (i,j) = (x,y),(y,x),(z,y), \text{ and } (y,z), \tag{5b}$$

$$P_n = \gamma^2(1 - \beta \cdot I^2 \cdot \lambda^2)^2\, T_{ij} \quad \text{for } (i,j) = (y,y). \tag{5c}$$

The difference between the three cases is a result of the measurement configuration. For measurements with polarization in the x-z plane, the precession coils are not turned on and therefore no dephasing or coupling factor is involved. For a measurement that involves a y component, the precession coils are turned on to precess the neutron polarization from $\hat{x}$ to $\hat{y}$, which introduces the field coupling and dephasing into the measured results.

The test experiment was performed at the HB-2D beamline at HFIR. Shown in Figure 7(a) are the measured results for the four matrix components T_{yy}, T_{xx}, T_{xy}, and T_{yx} as a function of the current in the solenoid sample. These tensor elements describe neutron polarization in the x-y plane. They are fitted to a cosine and sine function, respectively, as shown in Fig. 7, to give $T_{yy} = T_{xx} = \gamma_{solenoid} \cdot \cos[\omega_{solenoid} I]$ and $T_{xy} = -T_{yx} = \gamma_{solenoid} \cdot \sin[\omega_{solenoid} I]$, where $\gamma_{solenoid} = 0.99 \pm 0.005$ and $\omega_{solenoid} = 4.39 \pm 0.003$. These results show that the four components are the four precession terms in a rotation matrix around $\hat{z}$, as expected. Moreover, the oscillation angular frequency is consistent with the calculated result using the field strength in the sample solenoid calculated from Ampere's law. $\omega = (\gamma_L m/h) \cdot l\lambda \cdot (B/I) = 4.395$. However, after dividing out the dephasing and coupling factors, there is still a 0.1% depolarization, which indicates that the solenoid is not strictly

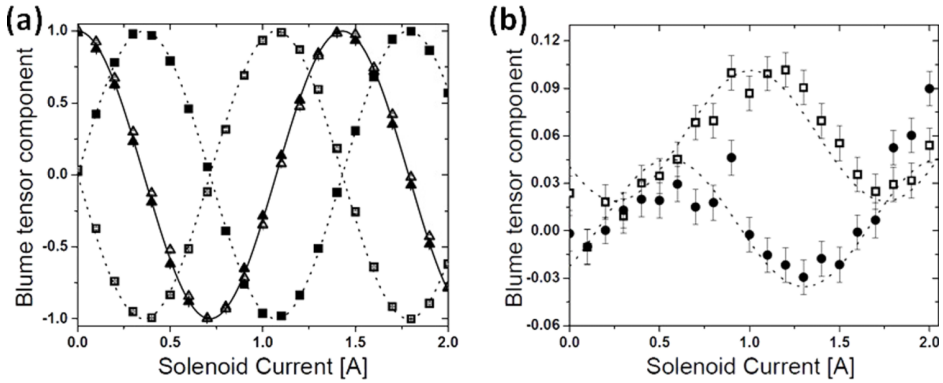

FIG. 7. (a) Sample matrix elements T_{xx} (solid triangles), T_{yy} (open triangles), T_{yx} (solid squares), and T_{xy} (open squares) measured for the solenoid sample. The lines are fits to cosine and sine functions. (b) Sample matrix component T_{zx} (solid circles) and T_{zy} (open squares) measured for the solenoid. The dashed lines are fits to the calculated matrix elements under the assumption that the solenoid is tilted.

parallel to the precession field direction ($\hat{z}$) and therefore causes a small part of the polarization to be transferred from the x-y plane to $\hat{z}$. The leakage of polarization from the x-y plane into $\hat{z}$ appears as non-zero T_{zx} and T_{zy} terms, which are shown as a function of solenoid current in Figure 7(b). Both T_{zx} and T_{zy} show oscillations with the same period as T_{xx}, indicating that the polarization along $\hat{z}$ is indeed transferred from the x-y plane by the solenoid field. The T_{xz} and T_{yz} results are essentially the same as T_{zx} and T_{zy} and therefore are not shown for clarity. As the transfer is a result of the solenoid field not being parallel to the precession field, we can estimate the tilting angle. Assuming the solenoid is tilted in the x-z plane by an angle ξ_1 and in the y-z plane by an angle ξ_2, the rotation axis of the solenoid is $u = [\sin(\xi_1), \sin(\xi_2), \cos(\xi_3)]$, where $\cos(\xi_3) = (1 - \sin^2(\xi_1) - \sin^2(\xi_2))^{1/2}$. Written in explicit form, the theoretical values of T_{zx} and T_{zy} are

$$T_{zx} = \cos(\xi_3)\sin(\xi_1)[1 - \cos(\omega I)] + \sin(\xi_2)\sin(\omega I), \quad (6a)$$

$$T_{zy} = \cos(\xi_3)\sin(\xi_2)[1 - \cos(\omega I)] - \sin(\xi_1)\sin(\omega I). \quad (6b)$$

Fits of the measured T_{zx} and T_{zy} results to Eq. (6) are shown as the dashed lines in Figure 7(b). The fitting results show that $\sin(\xi_1) = -0.01$ and $\sin(\xi_2) = 0.04$, which means that the solenoid is tilted towards $\hat{y}$ by 2° and tilted towards $-\hat{x}$ by 0.6°. From the estimated value of ξ_1 and ξ_2, one can calculate that $\cos(\xi_1) = 0.9994$ in agreement with a measured value of $T_{zz} = 0.99 \pm 0.01$. These results indicate the degree of accuracy that can be obtained, even with a simple device.

B. Polychromatic measurement

When multiple neutron wavelengths are used, as they typically are at a pulsed neutron source, it is impossible to manipulate all neutrons to the same vector polarization with a static precession field. One possible solution is to ramp the precession field synchronously at the pulse frequency of the source. However we have not been able to achieve this with our system because the precession fields behave in a complicated manner when the current is changed quickly. Nevertheless, in the case of the sample solenoid, the correlation described by Eq. (1b) is still valid. Therefore, instead of measuring single elements of the sample matrix as we do in the monochromatic case, we measure linear combinations of the matrix elements at a pulsed source and it is still possible to extract information.

An experiment to test this approach was performed at the SESAME beamline at LENS using the same sample solenoid as described above (including the tilting). Four of the sample matrix elements can be measured directly because the polarization is prepared using the rotatable guide fields alone and no precession is involved,

$$P_n = T_{ij} \quad \text{for } (i,j) = (x,x),(x,z),(z,x), \text{ and } (z,z). \quad (7a)$$

For measurements that require either the incoming or outgoing polarization to be along $\hat{y}$ (beam direction), one of the precession devices needs to be turned on. In this case, the normalized polarization from the measurements becomes a linear combination of the desired Blume tensor components (T_{ij}), the precession due to the precession field, and one of the tensor components measured in Eq. (7a),

$$P_n = \gamma^2(1 - \beta I^2\lambda^2)[\sin(\alpha I\lambda)T_{ij} + \cos(\alpha I\lambda)T_{zx}] \quad \text{for } (i,j) = (z,y), \quad (7b)$$

$$P_n = \gamma^2(1 - \beta I^2\lambda^2)[-\sin(\alpha I\lambda)T_{ij} + \cos(\alpha I\lambda)T_{xz}] \quad \text{for } (i,j) = (y,z), \quad (7c)$$

$$P_n = \gamma^2(1 - \beta I^2\lambda^2)[-\sin(\alpha I\lambda)T_{ij} + \cos(\alpha I\lambda)T_{xx}] \quad \text{for } (i,j) = (y,x), \quad (7d)$$

$$P_n = \gamma^2(1 - \beta I^2\lambda^2)[\sin(\alpha I\lambda)T_{ij} + \cos(\alpha I\lambda)T_{xx}] \quad \text{for } (i,j) = (x,y). \quad (7e)$$

And finally, to measure T_{yy}, both precession devices need to be turned on. The normalized polarization is a complicated combination of precessions due to both precession fields and Blume tensor components measured through Eqs. (7a)–(7e),

$$P_n = \gamma^2(1 - \beta I^2\lambda^2)^2[-\sin(\alpha I_1\lambda)\sin(\alpha I_2\lambda)T_{yy} - \cos(\alpha I_1\lambda)\sin(\alpha I_2\lambda)T_{yx} + \sin(\alpha I_1\lambda)\cos(\alpha I_2\lambda)T_{xy} - \cos(\alpha I_1\lambda)\cos(\alpha I_2\lambda)T_{xx}]. \quad (7f)$$

Equations (7a)–(7f) allow one to extract all Blume tensor components. The T_{zx} element measured in Eq. (7a) is also involved in Eq. (7b) and therefore must be determined first so that the T_{zy} term can be solved. The same goes with Eqs. (7c)–(7e) for extracting the T_{yz}, T_{yx}, and T_{xy} terms. Only

when all other elements have been determined can the last element, T_{yy}, be solved through Eq. (7f).

A limitation to this method arises at wavelengths where the sine terms become very small. For example, when $\sin(\alpha I\lambda) = 0$, the T_{yz} term vanishes in Eq. (7b) and this component of the sample matrix cannot be determined. For a static magnetic field, this singularity happens at certain wavelengths where the precession field puts the incoming neutron polarization in the $\hat{x}$ direction. At these specific wavelengths, there are no incoming neutrons with polarization in the $\hat{y}$ direction and T_{yz} term does not contribute to the measured result. To overcome this problem, we only need to change the current so that the singularity appears at a different wavelength. The same philosophy applies to the determination of other elements in Eqs. (7b)–(7f).

Shown in Figure 8 are the measured matrix element T_{xx} and the derived matrix element T_{yx} based on Eq. (7d), with these data fitted to the corresponding cosine and sine functions from the rotation matrix. The fitted results are $T_{xx} = 0.99\cos(1.93\lambda)$ and $T_{yx} = 0.99\sin(1.93\lambda)$. Once again the fitted precession frequency agrees with the value calculated from Ampere's law $\omega_\lambda = 1.93$ rad/Å. Notice for the T_{yx} measurement, the error of the measurement becomes large around 4 Å, which is the wavelength at which the sine term is close to zero. The T_{zz} measurement yields a result of 1.0 ± 0.01 across all neutron wavelengths, which is expected as for the T_{zz} measurement the neutron polarization is almost parallel to the sample solenoid field and therefore should be preserved.

As the sample solenoid is in the same configuration as for the monochromatic measurement described above, we would expect the same transfer of polarization from the x-y plane into the $\hat{z}$ direction and vice versa. This "leakage" is once again measured through the off-diagonal terms T_{zx} and T_{zy}. However, even though the measured off-diagonal results are roughly consistent with the monochromatic results, the statistics are not good enough to draw a clear conclusion. Such difficulty in determining the off-diagonal term accurately is not surprising, since the term is close to zero and the LENS beam intensity is very much less than that at HFIR. It is worth noting that, in addition to yielding that same results as those obtained with monochromatic neutrons, multiple wavelengths may yield additional information. For example, in the case that a sample causes both depolarization and rotation of the incident polarization, measurement with a single neutron wavelength will see a reduction of neutron polarization and be unable to distinguish its cause. For a polychromatic beam, the polarization rotation caused by the sample appears as an oscillation of the measured polarization while the depolarization causes a decrease of the oscillation magnitude. In addition, there also exists a limitation on whether the method can be applied. The approach of Eqs. (7b)–(7f) requires the measured Blume tensor to be independent of the incident polarization, which inevitably limits the application of the method in some scattering experiments.

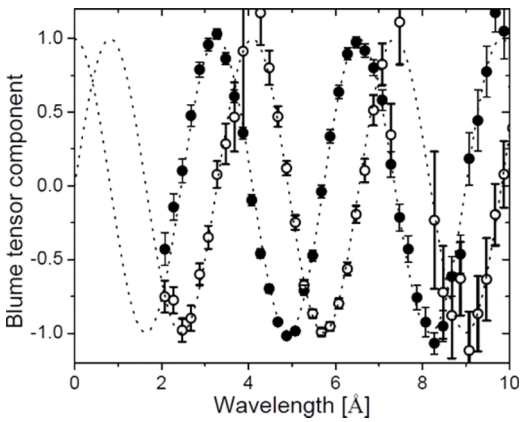

FIG. 8. Sample matrix elements T_{xx} (solid circle) and T_{yx} (open circles) measured for the solenoid sample with multiple wavelengths. The lines are fits to the calculated matrix components as described in the text.

V. MEASURING MAGNETIZATION OF A PERMALLOY FILM

Through the solenoid measurements, we were able to verify that our device works properly with both monochromatic and polychromatic neutron beams. As a further proof of principle, we performed a transmission measurement on a 10 μm thick Permalloy film. Permalloy is a nickel-iron magnetic alloy with high permeability and very little residual magnetization. In thin film form, its magnetization under external field is parallel to the film plane.[35] This transmission measurement was performed at the HB-2D beamline at HFIR.

The Permalloy film we used was synthesised by electrochemical deposition and has an in-plane easy axis. The sample was mounted on a 1/16 in. thick aluminium sample holder with the film in the x-z plane and placed inside the sample solenoid described above. The easy axis of the sample is in the $\hat{x}$ direction, perpendicular to the solenoid field direction. The sample was first measured in a zero field environment and all nine matrix elements are measured. Then we gradually increased the current applied through the sample solenoid and measured the precession of the neutron polarization.

A. Permalloy magnetization in zero magnetic field

Before the measurement, the sample was cooled down to 20 K in zero magnetic field and then degaussed by applying an oscillating magnetic field of decreasing magnitude. The measured sample matrix at zero-field is found to be

$$T_{Permalloy} = \begin{bmatrix} 0.982 \pm 0.004 & -0.066 \pm 0.006 & 0.041 \pm 0.006 \\ 0.053 \pm 0.006 & 0.434 \pm 0.005 & 0.034 \pm 0.006 \\ 0.038 \pm 0.006 & -0.002 \pm 0.006 & 0.435 \pm 0.002 \end{bmatrix}. \quad (8)$$

All six off-diagonal terms are close to zero indicating that very little neutron polarization is transferred from one direction to another. This result implies that in the remnant state the Permalloy film has no macroscopic magnetization. Otherwise the neutron polarization will precess around the magnetization and causes distinct non-zero off-diagonal terms. Among the three diagonal terms, T_{xx} is very close to unity while T_{yy} and T_{zz} are both non-zero and equal to each other within error. The

close-to-unity T_{xx} term indicates that neutron polarization in the $\hat{x}$ direction is preserved when neutrons pass through the sample. This means that magnetic domains are magnetized in the $+\hat{x}$ and $-\hat{x}$ directions, along the known orientation of the easy axis. Moreover, since there is no macroscopic magnetization, the magnetization in the + and $-\hat{x}$ directions must be equal.

In this case, all measured results can be interpreted as an average over two anti-parallel magnetizations along the easy axis. Notice for neutron polarization in the y-z plane, magnetization along $+\hat{x}$ and $-\hat{x}$ causes the neutron polarization to precess clockwise and counter-clockwise, respectively. As a result, the off-diagonal term $T_{zy} = T_{yz} = [\sin(\phi) + \sin(-\phi)]/2 = 0$, while $T_{yy} = T_{zz} = [\cos(\phi) + \cos(-\phi)]/2 = \cos(\phi)$, where ϕ is the phase angle of precession caused by the magnetization. Using $\cos(\phi) = 0.435$ from the measured T_{yy} *and* T_{zz}, we can therefore derive the magnitude of the magnetization at zero field,

$$M_{B=0} = \arccos(0.435)/[(m\gamma_l/h) \cdot \lambda d] \approx 9100 \text{ G}. \quad (9)$$

The calculated zero field magnetization in Eq. (9) is close to the saturation magnetization of Permalloy film, which is 9700 G, as measured by a SQUID device at 20 K. This result indicates that at zero field, the Permalloy film is still strongly magnetized along the easy axis on the microscopic scale, with equal populations of oppositely magnetized domains. Magnetic force microscope (MFM) characterization conducted by other research groups[36] has demonstrated that Permalloy film indeed has a maze domain pattern. From the obtained MFM image, the maze domain pattern consists of two types of domain with a size of 1–10 μm, which is infinitesimal compare to our experiment beam size of 5×8 mm^2 and the sample size of 10×12 mm^2. This is consistent with our observation of the magnetization. As the neutrons pass through the Permalloy sample perpendicular to the film, our experiment results also suggest that the maze domain structure extends through the film. Otherwise, the neutron would pass through multiple domains with opposite magnetizations, causing the overall precession angle to be reduced.

Still, the difference between the derived domain magnetization and the saturation magnetization cannot be explained clearly. It is possible that the domain walls are not precisely orthogonal to the film plane so that neutrons pass through two adjacent domains. Moreover for a single wavelength measurement it is impossible to distinguish depolarization and precession, as they both reduce the measured neutron polarization. This problem could be solved by instead using polychromatic neutron, in which case the precession causes an oscillation of the measured neutron polarization.

B. Precession inside a Permalloy film in an external magnetic field

To examine the response of the Permalloy film to an external magnetic field, we used the sample solenoid to apply a varying uniform magnetic field along the z direction, perpendicular to the easy axis of the Permalloy film sample. Both incoming and outgoing neutron polarizations are set to the x direction. In this case, the measured polarization $P = T_{xx} = \cos(\phi)$, where ϕ is the angle of precession in the x-y plane. For this measurement, we compared the amount of precession with and without the Permalloy sample inside the sample solenoid. For the same current applied through the sample solenoid, the difference in the phase angle is the result of additional precession caused by the Permalloy film.

The amplitude of the measured Blume tensor T_{xx} with the Permalloy sample is almost the same (close to unity) as with the solenoid (Figure 9(a)), showing the sample causes little depolarization. However, the precession of the neutron polarization with the Permalloy film is larger than with the solenoid alone. A plot of precession phase angle as a function of external field is shown in Figure 9(b), providing a clear picture of the magnetization saturation inside the Permalloy film. As shown in Figure 9(b) with increasing external field, the Permalloy film generates additional precession phase as a result of its increasing magnetization. The phase difference becomes constant at 7.5 G external field with a difference of 41°, which indicates that the magnetization inside Permalloy film is close to saturation. The magnetization can be calculated using

$$M_{B=7G} = \arccos(41^{\circ})/[(m\gamma_l/h) \cdot \lambda d] \approx 5900 \text{ G}. \quad (10)$$

This magnetization behaviour was checked using a SQUID magnetometer which showed that the Permalloy film

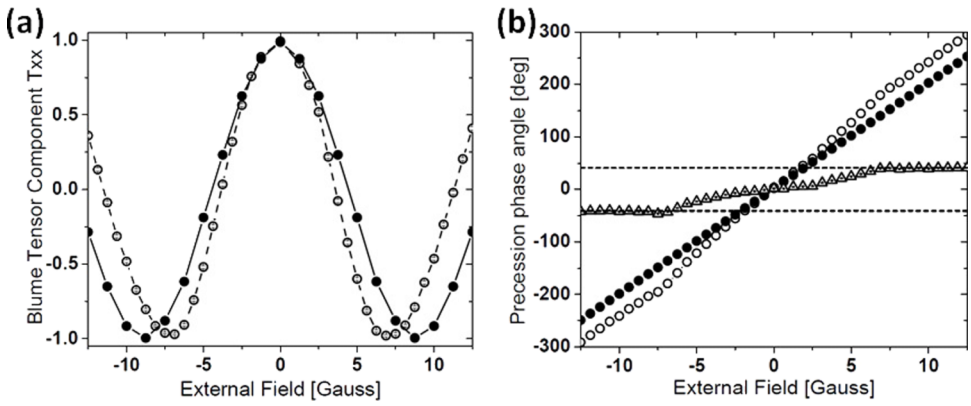

FIG. 9. (a) Comparison between the measured neutron polarization as a function of magnetic field with (open circles) and without the Permalloy sample (solid circles). (b) Comparison between the precession phase angle with (open circles) and without the Permalloy sample (solid circles) inside the solenoid. The phase difference is calculated and shown as open triangles.

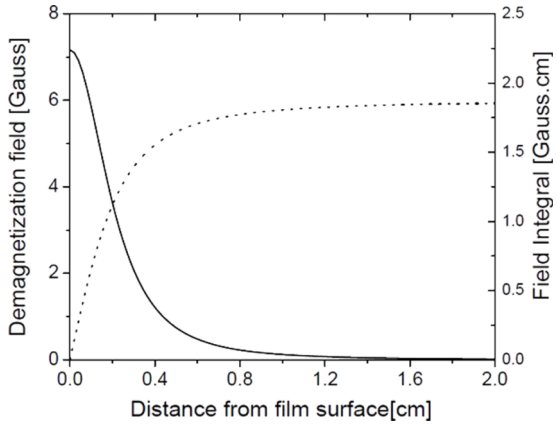

FIG. 10. Calculated demagnetization field strength as a function of distance to the Permalloy film (solid line) and the corresponding neutron precession field integral caused by this demagnetization field (dashed line).

has a magnetization of around 9500 G in a 15 G external field. The difference between the two results is due to the demagnetization field, which is opposite to the magnetization and the external field direction. For a thin film, the demagnetization field can be calculated along the neutron trajectory,[35] and the result is plotted in Figure 10.

As shown in Figure 10, the demagnetization field is only 7 G close to the film and quickly decreases to zero 1 cm away from the film. Such a field is small compared to the magnetization of 9500 G and therefore inaccessible for the SQUID measurement. However for the neutron measurement, the field due to the sample magnetization causes additional precession which is not negligible. For a field integral of 1.85 G·cm on each side of the film (Fig. 9), the demagnetization field contributes about −26° of precession to the measured phase difference. Therefore, the actual polarization rotation caused by magnetization inside the Permalloy film is in fact ~67°, which corresponds to 9485 G magnetization at 15 G external field, consistent with our SQUID measurement.

VI. DISCUSSION

The device we have made is functionally similar to CryoPAD,[16] at least for scattering at small angles, but has the advantages that it is both inexpensive to build and simple to operate; CryoPAD is capable of controlling the neutron polarization with a precision of 0.02° for precession and 0.01° for nutation.[31] The accuracy of precession of our device is determined by the current applied through the coils provided by the power supplies. For a typical 0.1 mA resolution, the precession accuracy is 0.005° at 4 Å. However, the nutation precision of our device is only 1°, limited by our ability to align the external guide fields accurately as shown in the calibration section. As for maintaining a zero-field sample environment, our device ensures less than 4 mG field within the sample chamber, which generates 0.04° of precession for 4 Å neutrons. CryoPAD generates 0.1° precession per 1 mG and usually measures a field of 1–3 mG inside the chamber. The lower amount of precession inside our device is due to its smaller sample chamber (6.6 cm), in comparison to the Ø37 cm CryoPAD chamber. Finally, the rotatable guide field on our device ensures adiabatic transport down to 1.6 Å while CryoPAD ensures adiabaticity down to 0.4 Å due to a much higher guide field magnitude. Although the accuracy with which polarization orientation can be controlled is usually the metric used to compare SNP devices, it is worth noting that these parameters do not necessarily represent the accuracy of "real-life" SNP scattering measurements. This arises partly because the various polarization rotations do not commute and partly because calibration of the device is almost never accomplished in exactly the same conditions as are used for an actual measurement. Nevertheless, these parameters provide confidence that our device is capable of performing SNP measurement with an accuracy similar to that achieved by existing devices.

Nowadays, most SNP measurements operate with a monochromatic neutron beam. We have shown that our device can be used as a zero-field polarimeter for both monochromatic and polychromatic beams. Compared to monochromatic measurements, the obvious advantage of polychromatic measurements is providing more information. However, the additional information comes with a price. Polychromatic measurement spreads out the beam over a range of neutron wavelengths and therefore requires much higher neutron flux to reach the same statistical accuracy. This statistical difference is non-trivial, especially considering that the off-diagonal terms are often small. Furthermore, the statistical uncertainty can be exacerbated in real measurements because some information (such as T_{yy} described in Section IV B) cannot be acquired until other terms in the matrix have been measured. The removal of the singularity point also requires multiple measurements of the same term. Moreover, it should be noticed that our approach in Section IV B is limited to small angle geometry and can only be used with a sample in which there are no nuclear-magnetic interaction terms or magnetic chirality. The restriction to small angles arises because the method requires a set of Blume tensor components to be measured first without using precession manipulation of the neutron spin. The other limitations arise because the method only works if the components of the Blume tensor are independent of the incident neutron polarization. A practical design for wide angle time-of-flight SNP measurement has been presented by Lelièvre-Berna[28] on the base of CryoPAD design, which replaces the nutator for outgoing neutron with another precession region. If the precession fields can be ramped synchronously with the neutron pulse in a TOF measurement, both TOF-CryoPAD and our device can, in principle, determine the full Blume tensor, at least for elastic scattering. However, such field ramping has not yet been demonstrated for either devices.

CryoPAD supports wide angle measurements and has dedicated sample environment control system, and therefore has a wide range of applications. Our current design implements SNP measurements over a limited range of scattering angles. The application in transmission geometry is shown in Section V. The device can also be applied to SANS and reflectometry to study the magnetic interactions and resolve three-dimensional magnetism. Compared to the existing polarization analysis small angle neutron scattering[15] (PASANS) and polarized neutron reflectometry (PNR) set-ups, our device

has the advantage of a zero field environment for the scattering sample which allows the analysis for off-diagonal terms in the Blume tensor. A similar device using resistive precession coils has recently been reported for the study of the helimagnetic transition[18] in MnSi. Neutron magnetic imaging is another possible application of the device, in which transmission images reveal regions of different magnetic field distributions.[37] Our device is designed with a zero field sample chamber, which removes the need for a magnetic guide field at the sample when imaging using polarized neutron. On the other hand, in our present device, the sample temperature cannot be independently controlled, which restricts the range of sample temperatures to be between 20 K and approximately 80 K.

VII. CONCLUSION

We have constructed a compact, inexpensive SNP device using superconducting YBCO components and a closed-cycle refrigerator. The device is capable of providing a zero field sample environment over a temperature range from 20 K to 80 K while manipulating both incoming and outgoing neutron polarizations. The performance and accuracy of the device have been characterized through calibration and two test measurements. Results obtained with a Permalloy film reveal the magnetic domain structure in the remnant state and agree with SQUID measurements when a magnetic field is applied.

ACKNOWLEDGMENTS

The design and construction of the device were supported by the National Science Foundation through Grant No. DMR-0956741. Construction of LENS was supported by the National Science Foundation Grant Nos. DMR-0220560 and DMR-0320627, the 21st Century Science and Technology fund of Indiana, Indiana University, and the Department of Defence. Operations of LENS are supported by the Office of the Vice Provost for Research at Indiana University. Measurement time on the HB-2D beamline at the HFIR at Oak Ridge National Laboratory (ORNL) is managed by UT-Battelle, LLC under Contract No. DE-AC05-00OR22725 with the U.S. Department of Energy.

[1]T. Chatterji, *Neutron Scattering from Magnetic Material* (Elsevier, 2005).
[2]R. M. Moon, T. Riste, and W. C. Koehler, Phys. Rev. **181**(2), 920 (1969).
[3]P. J. Brown, Physica B **297**(1-4), 198 (2001).
[4]S. V. Maleyev, Physica B **267**, 236 (1999).
[5]M. Blume, Phys. Rev. **133**(5A), 1366 (1964).
[6]O. Halpern and M. H. Johnson, Phys. Rev. **55**, 898 (1939).
[7]C. Pappas, E. Lelievre-Berna, P. Falus, P. M. Bentley, E. Moskvin, S. Grigoriev, P. Fouquet, and B. Farago, Phys. Rev. Lett. **102**(19), 197202 (2009).
[8]R. M. Moon and W. C. Koehler, J. Appl. Phys. **40**(3), 1454 (1969).
[9]R. M. Moon, J. Appl. Phys. **41**(3), 883 (1970).
[10]R. Pynn, W. G. Stirling, and A. Severing, Physica B **180**, 203 (1992); S. A. Werner, A. Arrott, and M. Atoji, J. Appl. Phys. **40**(3), 1447 (1969).
[11]R. M. Moon, J. W. Cable, W. C. Koehler, and H. R. Child, Phys. Rev. B **5**(3), 997 (1972).
[12]F. Mezei and P. A. Dagleish, Commun. Phys. **2**(2), 41 (1977).
[13]O. Scharpf, Physica B **182**(4), 376 (1992).
[14]O. Scharpf, T. Chattopadhyay, H. W. Weber, O. B. Hyun, and D. K. Finnemore, Phys. Status Solidi B **175**(1), 175 (1993).
[15]K. L. Krycka, R. Booth, J. A. Borchers, W. C. Chen, C. Conlon, T. R. Gentile, C. Hogg, Y. Ijiri, M. Laver, B. B. Maranville, S. A. Majetich, J. J. Rhyne, and S. M. Watson, Physica B **404**(17), 2561 (2009).
[16]F. Tasset, Physica B **156**, 627 (1989).
[17]M. Janoschek, S. Klimko, R. Gahler, B. Roessli, and P. Boni, Physica B **397**(1-2), 125 (2007).
[18]J. Kindervater, W. Haussler, M. Janoschek, C. Pfleiderer, P. Boni, and M. Garst, Phys. Rev. B **89**(18), 180408(R) (2014).
[19]P. J. Brown, J. B. Forsyth, and F. Tasset, Physica B **267**, 215 (1999).
[20]L. P. Regnault, F. Tasset, J. E. Lorenzo, T. Roberts, G. Dhalenne, and A. Revcolevschi, Physica B **267**, 227 (1999).
[21]A. Poole, B. Roessli, O. Zaharko, and K. W. Kramer, J. Phys.: Condens. Matter **23**(26), 266004 (2011).
[22]M. Janoschek, F. Bernlochner, S. Dunsiger, C. Pfleiderer, P. Boni, B. Roessli, P. Link, and A. Rosch, Phys. Rev. B **81**(21), 214436 (2010).
[23]C. M. Lavelle, D. V. Baxter, A. Bogdanov, V. P. Derenchuk, H. Kaiser, M. B. Leuschner, M. A. Lone, W. Lozowski, H. Nann, B. V. Przewoski, N. Rernmes, T. Rinckel, Y. Shin, W. M. Snow, and P. E. Sokol, Nucl. Instrum. Methods Phys. Res., Sect. A **587**(2-3), 324 (2008).
[24]M. Bendele, A. Maisuradze, B. Roessli, S. N. Gvasaliya, E. Pomjakushina, S. Weyeneth, K. Conder, H. Keller, and R. Khasanov, Phys. Rev. B **87**(6), 060409(R) (2013).
[25]M. TH. Rekveldt, J. Phys. Colloq. **32**(C1), C1–579 (1971).
[26]R. Maruyama, T. Ebisawa, S. Tasaki, M. Hino, M. Takeda, T. Kawai, Y. Kawabata, and K. Sakai, Physica B **335**(1-4), 238 (2003).
[27]W. Heil, K. H. Andersen, R. Cywinski, H. Humblot, C. Ritter, T. W. Roberts, and J. R. Stewart, Nucl. Instrum. Methods Phys. Res., Sect. A **485**(3), 551 (2002).
[28]E. Lelièvre-Berna, P. Bentley, E. Bourgeat-Lami, M. Thomas, C. Pappas, R. Kischnik, and E. Moskvin, Physica B **404**(17), 2624 (2009).
[29]S. R. Parnell, A. L. Washington, H. Kaiser, F. Li, T. Wang, W. A. Hamilton, D. V. Baxter, and R. Pynn, Nucl. Instrum. Methods Phys. Res., Sect. A **722**, 20 (2013).
[30]S. R. Parnell, H. Kaiser, A. L. Washington, F. Li, T. Wang, D. V. Baxter, and R. Pynn, Phys. Procedia **42**, 125 (2013).
[31]E. Lelievre-Berna, P. J. Brown, F. Tasset, K. Kakurai, M. Takeda, and L. P. Regnault, Physica B **397**(1-2), 120 (2007).
[32]D. V. Baxter, J. M. Cameron, V. P. Derenchuk, C. M. Lavelle, M. B. Leuschner, M. A. Lone, H. O. Meyer, T. Rinckel, and W. M. Snow, Nucl. Instrum. Methods Phys. Res., Sect. B **241**(1-4), 209 (2005).
[33]S. R. Parnell, A. L. Washington, K. Li, P. Stonaha, F. Li, T. Wang, A. Walsh, W. C. Chen, A. J. Parnell, J. P. A. Fairclough, D. V. Baxter, W. M. Snow, and R. Pynn, Rev. Sci. Instrum. **86**, 023902 (2015).
[34]G. L. Jones, F. Dias, B. Collett, W. C. Chen, T. R. Gentile, P. M. B. Piccoli, M. E. Miller, A. J. Schultz, H. Yan, X. Tong, W. M. Snow, W. T. Lee, C. Hoffmann, and J. Thomison, Physica B **385-386**, 1131 (2006).
[35]R. Pynn, M. R. Fitzsimmons, H. Fritzsche, M. Gierlings, J. Major, and A. Jason, Rev. Sci. Instrum. **76**(5), 053902 (2005).
[36]S. Getlawi, M. Theis, S. Friedrich, A. Koblischka-Veneva, M. R. Koblischka, M. Saumer, and U. Hartmann, Phys. Status Solidi A **205**(8), 1809 (2008).
[37]T. Shinohara, K. Sakai, M. Ohi, T. Kai, M. Harada, K. Oikawa, F. Maekawa, J. Suzuki, T. Oku, S. Takata, K. Aizawa, M. Arai, and Y. Kiyanagi, Nucl. Instrum. Methods Phys. Res., Sect. A **651**(1), 121 (2011).